SAND2006-4906C
Materials Science and Technology (MS&T), 2006

Joining of Superaustenitic Stainless Steels: A New Approach

T.D. Anderson[1], M.J. Perricone[2], J.N. DuPont[1]

[1]Lehigh University; Whitaker Laboratory, 5 East Packer Avenue; Bethlehem, PA 18015
[2]Sandia National Laboratories; P.O. Box 5800; Albuquerque, NM 87185

Keywords: stainless steel; phase transformations, filler metal; CALPHAD

Abstract

The non-uniform redistribution of critical alloying elements during weld solidification of superaustenitic stainless steels was alleviated through the use of an Fe-based filler metal that undergoes a ferritic primary solidification mode followed by a solid-state phase transformation to the austenite phase in order to match that of the base metal. This technique will improve weldability and corrosion resistance and lower costs relative to Ni-based filler metal solutions. Multi-component thermodynamic modeling was used isolate the range of available compositions. A set of experimental alloys was generated via the arc melting process in order to validate the calculations and locate possible filler metal compositions. EPMA traces confirmed the efficacy of this microstructural development sequence in redistributing critical Mo solute. Proper control of the weld composition and cooling rate will minimize the amount of residual ferrite and avoid the incidence of harmful σ-phase and martensitic transformation products.

Introduction

The use of superaustenitic stainless steel (SASS) alloys has been hampered by the lack of a suitable filler metal to aid in fusion welding. The high degrees of microsegregation inherent to the austenitic solidification have prevented Ni-based solutions from achieving high-quality welds[1,2]. The reduction of Mo at dendrite cores renders these areas prone to corrosive attack, while the segregation of tramp elements raises the susceptibility of the weld to solidification cracking. Previous research [3] has shown that the use of a ferritic primary solidification mode can help prevent solidification cracking of an austenitic stainless steel weld. This mode is possible because there exists a narrow range of near-eutectic compositions over which ferritic steel will experience a solid-state diffusional transformation to austenite during cooling due to the existence of a sloping solidus within the Fe-Ni-Cr phase diagram[4]. The weld zone can then match the austenitic crystal structure of the base metal. A new Fe-based filler metal is sought that will undergo this microstructural development sequence. The effect of composition was studied by generating a wide range of experimental alloys that were chosen through the use of thermodynamic calculations. Calculated phase diagram (CALPHAD) software can serve as an excellent tool for predicting alloy microstructure. The effect of this transformation on Mo distribution was investigated in order to estimate the resultant corrosion resistance properties the steel will have.

Experimental Procedure

Numerous vertical isopleths, such as that seen in **Figure 1a**, were constructed of the Fe-Ni-Cr-Mo system using the CALPHAD software Thermo-Calc[5] in conjunction with the Fe-Data Database[6]. While calculations were performed with Mo additions from 0- 10 wt%, the number of possible phases present was limited to three: liquid, ferrite, and austenite. These diagrams were used to generate composite phase stability diagrams that could be used to estimate the influence of alloy composition on the solidification mode, type of possible solid state transformation, and resultant microstructure. Laboratory studies were conducted in order to verify the accuracy of the diagrams in predicting microstructural development and observe alloys that exhibit the desired transformation sequence described above. A total of 96 alloys with systematic variations in Ni and Cr across both sides of the eutectic line in each nominal Mo contents modeled in Thermo-Calc were prepared. A master alloy of Fe-28Cr together with virgin Fe, Ni, and Mo were combined using an arc-button melter (ABM), provided by Thermal Technologies, Inc. The bell-jar of the ABM was evacuated and backfilled with Ar shielding gas. A manually-controlled gas tungsten arc torch running at 300A and 10V inside the chamber was manipulated to melt the elemental components on a water cooled Cu hearth. The ~50g buttons were subject to metallographic preparation and subsequent microstructural analysis in order to reveal and identify the particular solidification mode and solid-state transformation mechanisms. The relative locations and shape of the ferrite and austenite phases were used as indications of the solidification mode and morphological type in a manner previously described by Elmer [4]. A Feritscope, manufactured by Fischer Technology, Inc., was used to determine the specific weight percentage of ferrite within each alloy button. Precision was maintained through the use of calibrated standards of known ferrite content. Cell spacing measurements were used to estimate the cooling rate associated with the ABM and laser welding conditions. The relationships developed by Katayama and Matsunawa [7] for the primary dendrite arms of 310SS were used in this study on alloys of similar composition. Electron Probe Micro-Analysis (EPMA) was conducted on select alloys for each of the observed solidification modes in order to measure the distribution of each element within the microstructure. Raw data were converted to concentration values using the correction scheme devised by Heinrich [8].

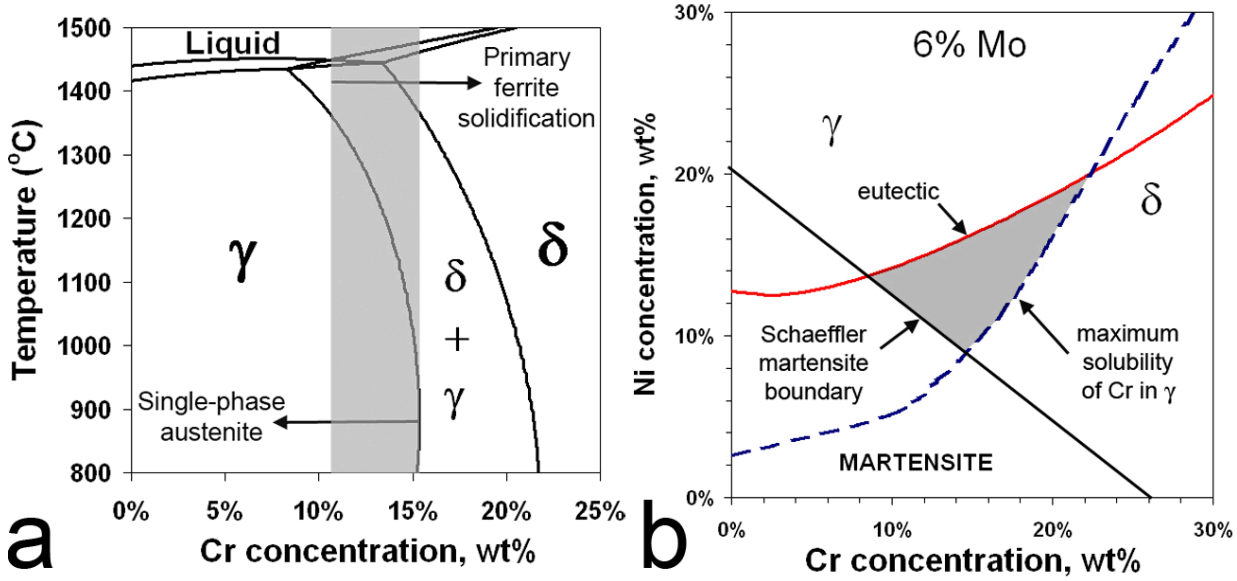

Figure 1. Separate views of the Fe-Ni-Cr-6Mo phase diagram: a) vertical isopleth at 69wt% Fe and 6wt%Mo; b) phase stability diagram highlighting Fe-Ni-Cr compositions with 6wt% Mo. The compositional zone of interest is highlighted in both diagrams.

Results and Discussion

Phase Stability Diagrams

Specific points of interest in the calculated vertical isopleths were used to generate the phase stability diagrams. As shown in Figure 1**a**, the compositions of the eutectic point and the maximum solubility of Cr in austenite were taken from pseudo-binary phase diagram at various concentrations of Fe. When plotted on the axes of Ni and Cr concentration, similar to a liquidus projection, these two points form lines that bound the range of compositions that can exhibit the two-stage microstructural development sequence desired in this research and are thermodynamically capable of a complete transformation to austenite. An example of the multi-component phase stability diagrams is shown in **Figure 1b**. The band across the center describes the three vertices of the eutectic triangle. The dashed line that intersects this band represents the maximum solubility of Cr in austenite, which curves below the eutectic triangle at high Cr and Ni concentrations. The initial requirement for the desired alloy development was that the primary solidification mode would be ferrite. In the absence of dendrite tip undercooling, compositions below and to the right of the eutectic line should undergo primary ferrite solidification. The second requirement for the alloy composition is that it experiences a complete solid-state phase transformation of ferrite into austenite, so the alloy must cool into a region of the phase diagram in which austenite is the only stable phase. As seen in the vertical isopleth in **Figure 1a**, there is a range of alloys that solidify as primary ferrite and can cool to a point at which austenite becomes stable. Alloys that cool into the $\delta + \gamma$ region will experience the solid-state $\delta \rightarrow \gamma$ phase transformation, but the transformation cannot go to completion. Compositions that enter the single-phase austenite region would see the most thermodynamic driving force to transform residual ferrite to austenite. This requirement allows for the maximum solubility of Cr in austenite to be deemed a secondary boundary.

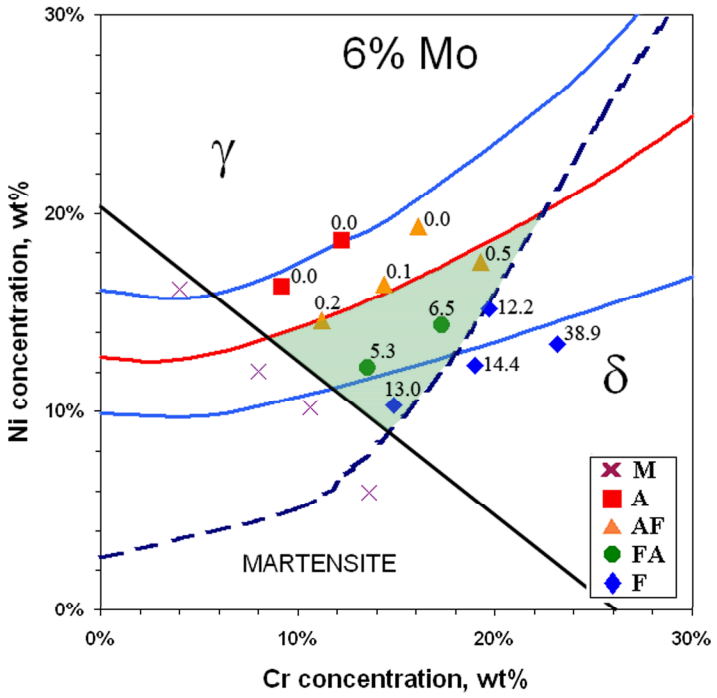

Figure 2. Multi-component phase stability diagram of the Fe-Ni-Cr-6Mo system. Data points represent experimental alloy compositions, with the shape of the data point signifying the observed solidification mode. The measured wt% ferrite for each composition is included alongside the respective data point.

Thermodynamic calculations can thus be used to bound compositions that have the thermodynamic potential to develop a final austenitic matrix that is preceded by ferrite solidification. Since the diagrams take into account only thermodynamic considerations, they are not proficient at predicting the type or amount of transformation that will occur. This factor can only be found through an analysis of the kinetics of the system, which takes into account the cooling conditions present. Therefore, the diagrams represent a necessary, but not sufficient, condition for attaining an austenitic matrix alloy derived by ferritic solidification.

Compositions that meet both requirements have been shaded for emphasis in both **Figure 1a** and **b**. The martensite line derived from the Schaeffler diagram is also provided for reference. The range of compositions that can be viewed simultaneously is far greater in this multi-component phase stability diagram than can be imaged in the vertical isopleth. An entire range of stainless steel compositions are

available for a single Mo content in the phase stability diagram. **Figure 2** shows a sample phase stability diagram generated in this study for the 6wt% Mo content. The data points represent the experimental alloys and are found at the Cr and Ni contents found via wet-chemistry analysis. The phase stability diagrams calculated in this research were validated using metallographic observations of each alloy. The type of solidification mode is denoted by the shape of the data point, while the corresponding weight percentages of ferrite phase are included beside each data point.

The calculated eutectic lines were fairly accurate in separating alloys between the austenitic and ferritic primary solidification modes, especially in the lower Mo diagrams. Nearly a third of the samples showed evidence of the martensite phase, as predicted by the Schaeffler Diagram. The first indication of the presence of martensite was given by the abnormally high magnetic signal in these alloys. The magnetic properties of martensite were the source of these measurements, and metallographic observations confirmed the presence of this phase. Since the martensite phase was not desirable in this particular application, microstructural analysis of these 31 alloys is omitted in order to maintain focus on alloys composed predominately of austenite. A future article [9] will discuss the myriad microstructural development sequences involving martensite that are possible in this alloy system. Of the 65 alloys that contained no martensite, only eight were found to disagree with the solidification modes predicted by the phase stability diagrams. In nearly all cases, their nominal compositions were very close to the calculated eutectic lines; these are likely the result of poor assumptions made during thermodynamic calculations.

Weld Metal Microstructures

A detailed description of the wide range of transformation sequences and resultant microstructures of the experimental alloys is presented elsewhere[9], and only a summary of the pertinent results will be provided here. The matrix of alloys was shown to contain each of the four common solidification modes exhibited by stainless steels: 1) austenitic (A); 2) austenitic-ferritic (AF); 3) ferritic-austenitic (FA); and 4) ferritic (F). A representative microstructure for each of these modes can be seen in **Error! Reference source not found.**.

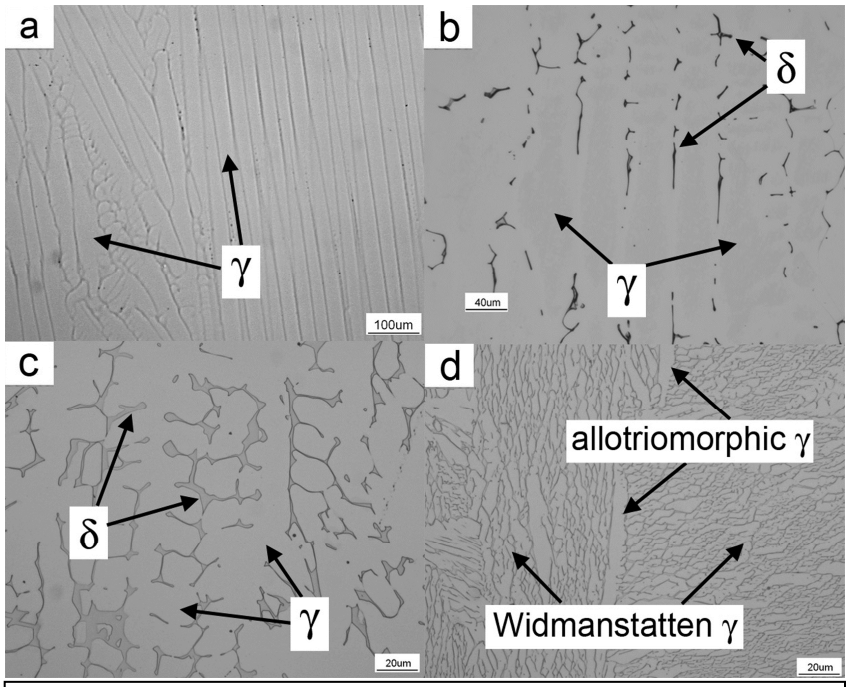

Figure 3. Representative microstructures of the four solidification modes observed in the set of alloys generated in this study: a) A: 0Mo-18Cr-17Ni-Fe; b) AF: 0Mo-18Cr-12Ni-Fe; c) FA: 2Mo-18Cr-12Ni-Fe; d) F: 2Mo-17Cr-8Ni-Fe.

The first two images in **Figure 3a** and **b** show alloys with austenitic primary solidification modes. The A mode alloy in **Figure 3a** is entirely austenite, while the AF mode alloy in **Figure 3b** contains interdendritic ferrite as a result of eutectic solidification.

The latter two solidification modes were of greatest importance in this study, since they fulfill the requirements set forth above. The difference between the two modes is the existence of austenite at the end of solidification. FA mode alloys exhibit this interdendritic austenite, from which the solid-state transformation of ferrite into austenite may ensue epitaxially [4]. A representative microstructure of the FA mode is shown in **Figure 3c**. The residual ferrite seen in the structure is located at what were

formerly the dendrite cores. Accordingly, the centerline of the austenite regions represents the former location of interdendritic regions. The compositions of all FA mode alloys were found to fall in the prescribed region of the phase stability diagram between the eutectic line and the maximum solubility of Cr in austenite.

The rest of the primary ferrite alloys belonged to the F mode group. An example of an F mode structure is shown in **Figure 3d**. Fully-ferritic grains were consumed by austenitic allotriomorphs at the grain boundaries, from which austenitic Widmanstatten side-platelets grew. Results of ferrite measurements indicate that this transformation mechanism is not as efficient as the FA mode at reducing the amount of residual ferrite. Eleven FA mode compositions were prepared; the ferrite contents were nearly all below that measured in the F mode samples.

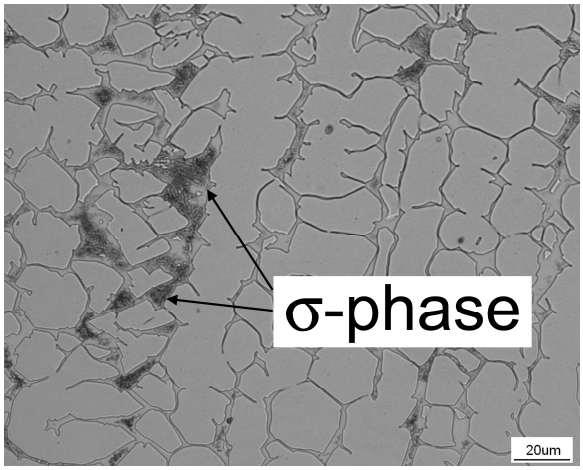

Figure 4. Representative microstructure of σ-phase as found in the FA mode structure of alloy 10Mo-18Cr-17Ni.

Of special note is the reduction in ferrite content in primary ferrite samples as the Mo content is increased. Indeed, several 10wt% Mo F mode samples contain less than 10wt% ferrite, and one FA alloy with 10wt% Mo produced a reading of 0wt% ferrite. Microstructural examination of these regions revealed the presence of another phase: the high Mo intermetallic σ-phase. Previous research has shown that a eutectoid σ/γ constituent may nucleate and grow from the parent ferrite phase[10,11]. This eutectoid structure is observed in every solidification mode that contained ferrite; an example can be seen in the FA mode in **Figure 4**. Phase identification of this phase was carried out through analysis of backscattered Kikuchi patterns [12]. Such a structure is typically associated with annealing heat treatments that expose stainless steel ferrite to elevated temperatures for long durations. The high Mo contents of these alloys coupled with the cooling conditions of the ABM were sufficient for this eutectoid transformation to occur. A more detailed inspection of this mechanism is available elsewhere [12].

Observations of the microstructure and measurements of the austenitic cell spacings revealed that the cell spacing increased across the height of the button. The region closest to the Cu hearth experienced the fastest cooling, which led to the smallest dendrites observed in the button. Accordingly, attempts were made to acquire all data from the central band of the button in order to report the average cooling rate within the entire button. The photomicrographs given in **Figure 3** are from the same region of the arc-melt button. The data indicates an average cell spacing of 26 microns, which represents

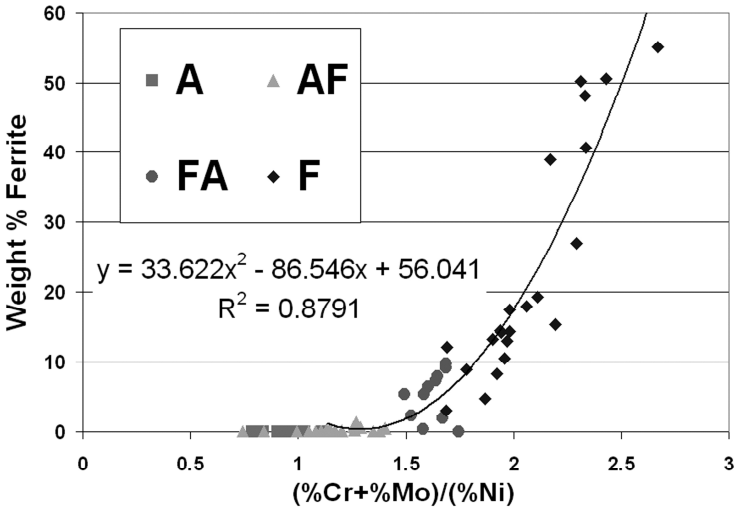

Figure 5. The effect of Cr_{eq}/Ni ratio on the measured weight percentage of ferrite. The data points are separated by the type of solidification mode.

an average cooling rate of 30 K/s. This figure is closer to the range of casting conditions (1-100 K/s) than the range typically reported [4] during arc welding (10-1000 K/s). Such a low cooling rate would facilitate the nucleation and growth of the γ/σ eutectoid structure.

Effects of Composition on Microstructure and Ferrite Content

As would be expected, the weight percentage of ferrite measured in the alloys increased as a function of Cr_{eq}/Ni (Cr_{eq} = wt% Cr + wt% Mo). The data is plotted in **Figure 5** with the alloys differentiated according to their solidification mode. The data indicates that each solidification mode belongs to a specific regime of Cr_{eq}/Ni ratio. The boundary between AF and FA mode alloys that is found at $1.5Cr_{eq}/Ni$ is in good agreement with previous findings [3]. Another significant boundary can be seen between FA and F mode alloys at $1.7Cr_{eq}/Ni$. This value is similar to the Cr/Ni limit that was reported for Mo-free alloys by Elmer, et al [4]. The plot also shows that the FA mode was far more efficient at reducing the amount of the primary solidified ferrite, as the detected ferrite content in F mode alloys ranged between 3 and 55wt%. Meanwhile, the ferrite content of FA alloys never surpassed 10wt%. A polynomial trendline has been included in this figure that relates the ferrite content to the Cr_{eq}/Ni ratio. Only those alloys with a detectable amount of ferrite were included in this relation.

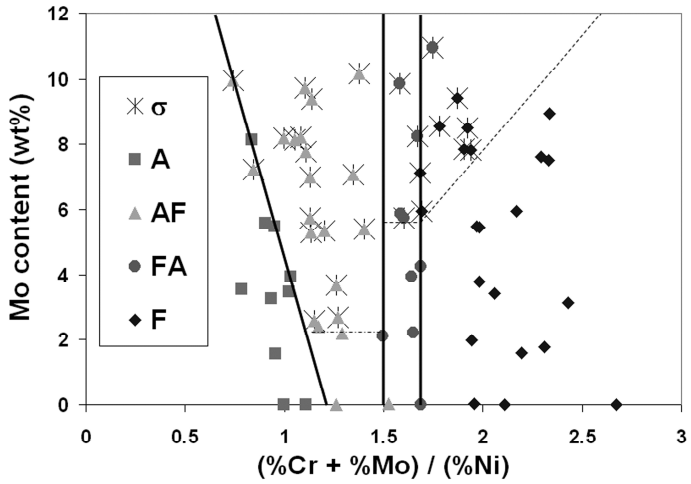

Figure 6. Microstructural map of alloy solidification mode based on Cr_{eq}/Ni ratio and Mo content. Boundaries are included to separate regions by solidification mode and σ-phase content.

The solidification mode and presence of σ-phase are mapped out as a function of Mo concentration and Cr_{eq}/Ni_{eq} ratio in Figure 6. As shown in **Error! Reference source not found.**, a switch in solidification mode from AF to FA occurs at a Cr_{eq}/Ni_{eq} ratio of 1.5. Also, the switch from FA to F mode is found at a Cr_{eq}/Ni_{eq} ratio of 1.7. Whereas the previous figure plotted all alloys by one compositional parameter (Cr_{eq}/Ni), **Figure 6** shows that the previously observed boundaries that separate solidification modes do not change as the Mo content is altered. These findings seem to indicate that the long-standing assumption that Mo possesses a ferrite-stabilizing strength equal to that of Cr is valid for the high Mo alloys. Boundaries are also included that separate σ-containing samples from σ-free samples. **Figure 6** thus represents a map by which microstructures may be predicted based on composition for a wide range of Mo-bearing stainless steels prepared under similar conditions. Of particular interest are the near-eutectic alloys with 4-6wt% Mo. Alloys that solidified in the AF mode showed substantial amounts of σ-phase that formed when the interdendritic ferrite decomposed to σ-phase via the $\delta \rightarrow (\sigma + \gamma)$ eutectoid type reaction. (Details of this transformation are provided in Ref. 12) On the other side of the eutectic, FA mode alloys showed no evidence of σ-phase up to 6 wt% Mo, save for a few isolated particles in the 6Mo-16Cr-14Ni sample. The lack of σ-phase in these 0-6 wt% Mo alloys implies that the Mo content was more uniformly distributed throughout the microstructure as opposed to residing in the interdendritic regions forming σ-phase. This is confirmed quantitatively in a later section.

Analysis of Data Using Accepted Stainless Steel Diagrams

Stainless steel constitution diagrams such as the Schaeffler Diagram or WRC-1992 Diagram have been derived empirically through examination of the ferrite content and phase balances of a vast array of stainless steel alloys of varying compositions. The large number of alloys presented herein is useful in assessing the accuracy of these diagrams for use with higher Mo stainless steels.

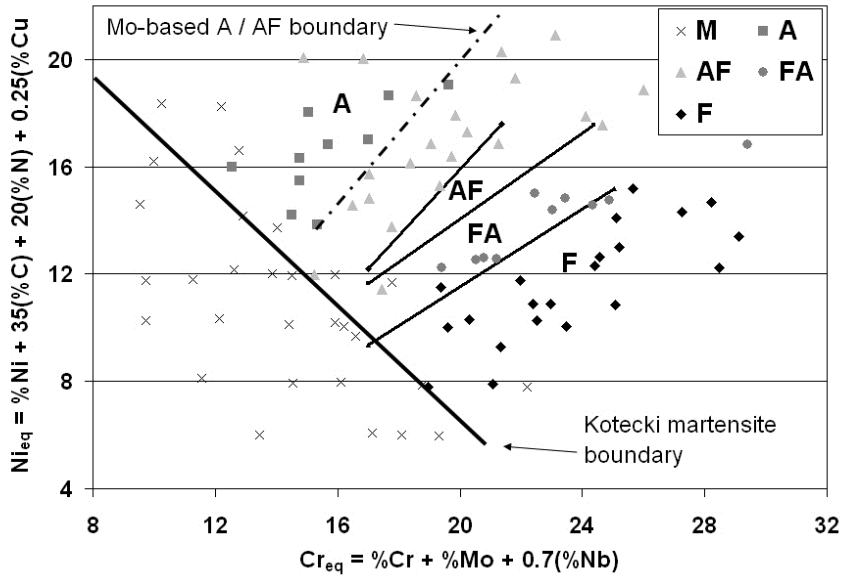

Figure 7. Experimental Fe-Ni-Cr-Mo alloys plotted on the WRC-1992 weld constitution diagram. Kotecki's proposed martensite boundary is given, as well as a new boundary to divide A mode from AF mode alloys.

The most modern constitution diagram in current research is the WRC-1992 diagram. The advantage of this diagram is its inclusion of boundaries which demarcate the various solidification modes available in the range of industrial stainless steels. **Figure 7** shows the entire set of experimental alloys plotted on the WRC-1992 diagram based on measured Cr and Ni equivalencies. Numerous AF mode samples can be seen in the region of the WRC-1992 diagram labeled as A. A majority of these alloys were high-Mo samples that contained σ-phase. If the Mo was not present to enable the eutectoid transformation, it is possible that the interdendritic ferrite would have otherwise transformed into austenite, in effect creating the fully austenitic structure predicted by the diagram. However, the low partition coefficient of Mo causes it to be highly segregated to the liquid. This in turn leads to a greater likelihood of forming interdendritic ferrite as compared to samples with equivalent amounts of Cr. Plotting the samples according to solidification mode on the WRC-1992 diagram (as in **Figure 7**) shows poor agreement between the predictions of the diagram and the experimentally observed solidification mode for primary austenite alloy compositions. The effects of Mo microsegregation are not accounted for in the WRC-1992 diagram, because the body of samples used in the initial design suffers from a lack of high-Mo samples. The list of original samples used [13] shows that only 4 samples contained greater than 5wt% Mo, the highest reaching 6.85wt% Mo. A new boundary is thus given in **Figure 7** to distinguish A and AF mode alloys with high Mo contents. Good agreement is shown, however, for primary ferrite alloys, since the bcc ferrite lattice is more amenable to backdiffusion of Mo solute.

Although previously included in the Schaeffler and DeLong diagrams, the WRC-1992 diagram does not include the martensite phase. The martensite boundary devised by Schaeffler in his diagram was superimposed on the stability diagrams shown above in **Figure 7**. This line was quite effective at separating martensite-free alloys from their martensite-containing counterparts. Recent research efforts have sought to locate a martensite line within the WRC-1992 diagram. Kotecki has proposed a martensite boundary [14] based mainly on the results of bend tests that is shown in **Figure 7**, in which the set of 96 alloys are also shown, plotted by their Cr and Ni equivalencies. The alloys which are known to form martensite can be used to validate the boundary proposed by Kotecki. Seven of the

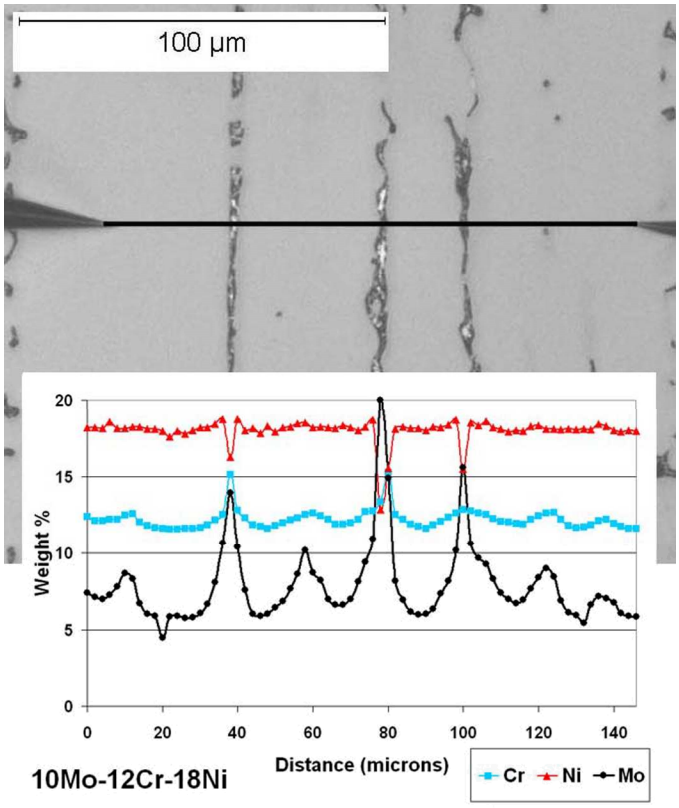

Figure 8. EPMA linescan data for austenite cells derived by solidification, with interdendritic ferrite and σ-phase, produced by the AF solidification mode.

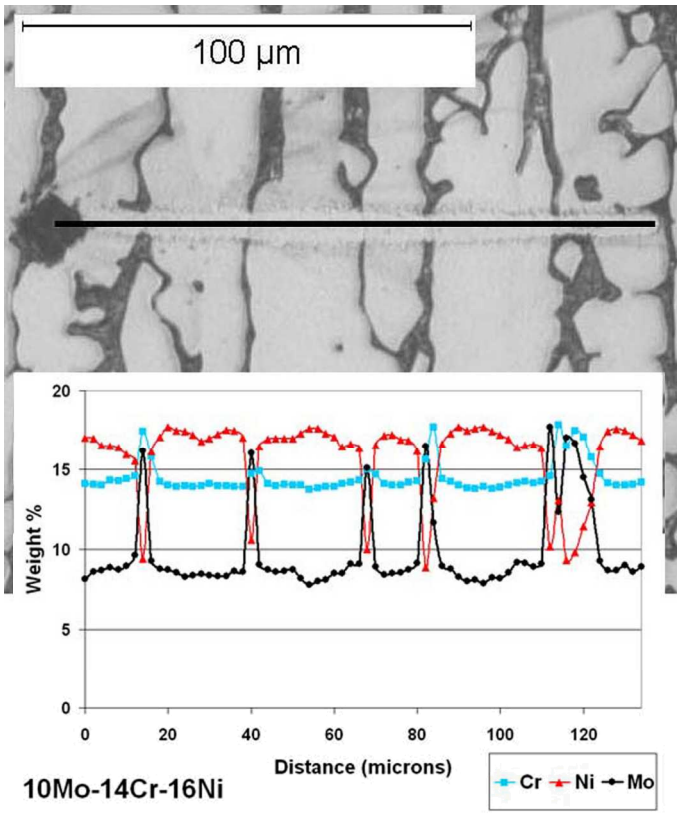

Figure 9. EPMA linescan data of austenite derived by solid-state transformation in the FA solidification mode. The residual ferrite has been consumed by the γ/σ eutectoid transformation.

martensitic samples from this study are actually located above this boundary. All of these samples contain at least 8wt% Mo. The origin of this behavior can again be explained by the high potential of Mo for microsegregation. Visual cues given in the microstructure show that martensite rarely occurs in the interdendritic regions, and is typically localized in the dendrite cores. Because of microsegregation, the Mo concentration at the core is actually less than the nominal composition. Therefore, the Ms temperature will be higher at the dendrite core. The incidence of martensite in these samples does not disagree with Kotecki's martensite boundary, since the true Mo concentration in the primary dendrite would be located to the left of the points demarcated in **Figure 7**.

Solute Redistribution

An example of the difference in solute profiles between alloys with similar Mo concentrations that form by AF and FA solidification are shown in **Error! Reference source not found.** and **Error! Reference source not found.**. Both contain high (~10wt%) concentrations of Mo, so the interdendritic (AF) or residual (FA) ferrite is consumed by the (γ+σ) eutectoid discussed above. However, the EPMA profiles are still indicative of the ferrite phase from which this structure originated. The Mo profile shows a definite increase in concentration in the distance between a cell core and the neighboring intercellular region produced by AF solidification. This was caused by the solidifying cell rejecting Mo into the liquid. The solute accumulates in the intercellular region, since it is the last to solidify. A

similar process occurs in the solidification of ferrite, with solute being rejected to the liquid. Owing to the improved diffusivity of solute in the open *bcc* structure of ferrite, Mo is able to diffuse down the concentration gradient towards the cell core. The transformed austenite regions in **Error! Reference source not found.** show a more uniform concentration of Mo. Since the central axis of the austenite regions represents the former intercellular regions of the solidified ferrite cells, it is established that the initial concentration gradient of Mo was significantly reduced via backdiffusion, prior to the $\gamma \rightarrow \delta$ transformation.

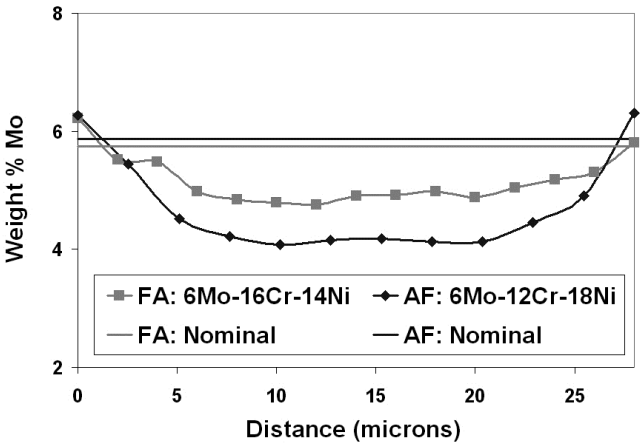

Figure 10. EPMA trace of the Mo content of a single austenite region. The AF trace consists of mostly solidified austenite, while the FA trace measures the Mo in both eutectic austenite and the austenite that grew epitaxially from it. The nominal Mo concentrations are also given for comparison.

The partitioning of Mo during the transformation is apparent by the high levels of Mo seen in the γ/σ-phase dual structure of Figure 9. As shown by peaks in the solute profile, the elements Cr and Mo, both stabilizers of the ferrite-phase, were rejected into the residual ferrite during the $\delta \rightarrow \gamma$ solid-state transformation process. The austenite matrix resulting from the FA solidification mode contains slightly less than nominal, yet essentially uniform, concentrations of these solute atoms. Conversely, austenite-stabilizing Ni was drawn into the newly created austenite, resulting in a uniform profile of Ni within the austenite that was greater than the nominal composition. As seen in **Error! Reference source not found.**, the residual ferrite was thus depleted of Ni.

Solute partitioning resulting from solid-state transformation does not, however, cause a chemical profile equivalent to that produced by microsegregation such as during AF solidification. **Error! Reference source not found.** compares the profile of Mo solute between a single solidified austenite cell brought about by AF solidification with a region of austenite derived by solid-state transformation within the FA solidification mode. While neither austenite region reaches the nominal concentration of ~6wt% Mo, the concentration in the FA austenite is certainly closer to 6wt% across its entire width. The advancing transformation front partitioned Mo to the remaining ferrite regions, where the excess Mo led to the formation of σ-phase, preventing the austenite regions from reaching the nominal level of 6wt% Mo.

Candidate Alloys

It is worth noting that several alloys investigated in this research exhibited the desired FA solidification mode, a low ferrite content, and no σ phase. Of the 65 alloys created that did not contain martensite, nine Mo-bearing alloys were identified that exhibited the FA solidification mode. Of these nine alloys, one contained 8 wt% Mo and two contained 10 wt% Mo. However, these three alloys all contained σ-phase. Since σ-phase is known for its unfavorable effects on mechanical properties and corrosion resistance [15], these three alloy compositions may not be optimal. The remaining six alloys, which are summarized in Table I, contain only 5-10wt% of the ferrite phase, as measured by magnetic instrumentation, and provide a basis for promising candidate compositions for further study.

Table I. Candidate alloy compositions for a filler metal for SASS alloy base metals.						
Designation	Fe	Ni	Cr	Mo	(Cr+Mo)/Ni	Wt% Ferrite
2Mo-18Cr-12Ni	66.31	12.60	18.55	2.22	1.648	7.93
2Mo-20Cr-15Ni	62.17	15.02	20.33	2.12	1.494	5.40
4Mo-17Cr-13Ni	66.59	12.51	16.57	3.95	1.640	7.31
4Mo-20Cr-15Ni	59.91	14.75	20.63	4.26	1.687	9.82
6Mo-13Cr-12Ni	68.06	12.23	13.53	5.87	1.586	5.33
6Mo-16Cr-14Ni	62.25	14.37	17.29	5.75	1.603	6.48

Summary and Conclusions

1) The phase stability diagrams constructed from thermodynamic calculations provided a good predictive tool of the microstructural development of Mo-bearing stainless steel alloys.

2) The ferrite content was shown to be a function of not only Cr_{eq}/Ni ratio, but also Mo concentration, due to the transformation of ferrite into eutectoid $\gamma + \sigma$ in high-Mo alloys.

3) The WRC-1992 weld constitution diagram accurately predicted the presence of martensite in low-Mo alloys. The high microsegregation of Mo led to martensite forming in high-Mo alloys that exceeded Kotecki's proposed martensite boundary.

4) The microsegregation of Mo was also held responsible for the location of numerous AF mode alloys in the A mode region of the WRC-1992 diagram. The high degree of σ-phase formation in the high-Mo samples also led in to inaccurate prediction of ferrite content.

5) The FA solidification mode produced a more uniform distribution of Mo solute in the transformed austenite phase than observed in the cores of solidified austenite cells produced by the AF mode. The average concentration of Mo in the FA austenite was also closer to the nominal concentration than in AF austenite.

6) Several candidate compositions for a filler metal for SASS alloys have been selected.

Reference List

1. S. Banovic, J. DuPont, and A. Marder, "Dilution and microsegregation in dissimilar metal welds between super austenitic stainless steel and nickel base alloys." *Science and Technology of Welding and Joining (UK)* **7**(2002), 374-383.
2. S. Banovic, J. DuPont, and A. Marder, "Microstructural Evolution and Weldability of Dissimilar Welds between a Super Austenitic Stainless Steel and Nickel-Based Alloys." *Welding Journal* **82**(2003, 125-135).
3. J. Brooks and A. Thompson, "Microstructural Development and Solidification Cracking Susceptibility of Austenitic Stainless Steel Welds." *International Materials Reviews* **36**(1991), 16-44.
4. J. Elmer, S. Allen, and T. Eagar, "Microstructural Development During Solidification of Stainless Steel Alloys." *Metallurgical Transactions A* **20A**(1989), 2117-2131.
5. B. Sundman. Thermo-Calc. S-100 44[[N]]. 2001. Stockholm, Sweden, Department of Materials Science and Engineering, KTH.
6. N. Saunders. Fe-Data Thermodynamic Database. [[3.0]]. 2001. The Surrey Research Park, Guildford, UK, Thermotech, Ltd.
7. S. Katayama and A. Matsunawa. Proceedings of ICALEO(1984), 60-67.
8. K.Heinrich,R.L.Myklebust,H.Yakowitz,and S.D.Rasberry. "Simple Correction Procedure for Quantitative Electron-Probe Microanalysis." NBS Technical Note 719(1972), 1-31.
9. T. Anderson, J. DuPont, M. Perricone, and A. Marder, "Phase Transformations and Microstructural Evolution of Mo-bearing Stainless Steels." *unpublished research* (2006).
10. W. Reick, M. Pohl, and A. Dapilha, "Recrystallization-Transformation Combined Reactions during Annealing of a Cold Rolled Ferritic-Austenitic Duplex Stainless Steel." *ISIJ International (Japan)* **38**(1998), 567-571.
11. C. Shek, G. Shen, J. Lai, and B. Duggan, "Early Stages of Decomposition of Ferrite in Duplex Stainless Steel." *Materials Science and Technology* **10**(1994), 306-311.
12. M. Perricone, C. Robino, T. Anderson, and J. DuPont, "On the Formation of Sigma in Mo-bearing Stainless Steels." *unpublished research* (2006).
13. D. Kotecki and T. Siewart, "WRC-1992 Constitution Diagram for Stainless Steel Weld Metals: a Modification of the WRC-1988 Diagram." *Welding Journal* **71**(1992), 171-178.
14. D. Kotecki, "A Martensite Boundary on the WRC-1992 Diagram." *Welding Journal* **78**(2000), 180-192.
15. T. Koseki and T. Ogawa, "An Investigation of Weld Solidification in Cr-Ni-Fe-Mo Alloys." *Welding International* **6**(1992), 516-522.